

CFD simulation of a high-shear mixer for food emulsion production

*Original*

CFD simulation of a high-shear mixer for food emulsion production / Ferrari, Marco; Boccardo, Gianluca; Buffo, Antonio; Vanni, Marco; Marchisio, Daniele L.. - In: JOURNAL OF FOOD ENGINEERING. - ISSN 0260-8774. - ELETTRONICO. - 358:(2023). [10.1016/j.jfoodeng.2023.111655]

*Availability:*

This version is available at: 11583/2981609 since: 2023-09-04T16:12:54Z

*Publisher:*

Elsevier

*Published*

DOI:10.1016/j.jfoodeng.2023.111655

*Terms of use:*

This article is made available under terms and conditions as specified in the corresponding bibliographic description in the repository

*Publisher copyright*

(Article begins on next page)

# CFD simulation of a high-shear mixer for food emulsion production

Marco Ferrari<sup>a</sup>, Gianluca Boccardo<sup>a,\*</sup>, Antonio Buffo<sup>a</sup>, Marco Vanni<sup>a</sup> and Daniele L. Marchisio<sup>a</sup>

<sup>a</sup>Department of Applied Science and Technology, Politecnico di Torino, Corso Duca degli Abruzzi 24, Torino, 10129, Italy

---

## ARTICLE INFO

### Keywords:

Mayonnaise  
Cone mill  
CFD-PBM simulations

## ABSTRACT

Mayonnaise is a stable liquid-liquid emulsion with high content of the disperse oil phase. In the last step of its production, the emulsion is fluxed into a high-shear mixer, where the oil droplets undergo breakage until the final size distribution is reached. This step is crucial to fine-tune the droplet size distribution (DSD), in order to result into the desired structure, stability, taste and color. In this work, we aim to model this last step via computational fluid dynamics (CFD) and population balance modelling (PBM), to properly describe both the non-Newtonian dynamics of the emulsion and the evolution of the DSD. 2D and 3D CFD simulations show that attention should be paid to the grid resolution to properly describe recognizable patterns observed in experiments. Moreover, CFD and PBM simulations clarify the role of the pre- and post-mixing zones in the high-shear mixer, as well as the effect of the type of flow, pure shear vs elongational, on droplet breakage. This effort is carried out in the context of the VIMMP project ([www.vimmp.eu](http://www.vimmp.eu)) where this work will contribute to populate a marketplace for generic multiscale and multiphysics simulations.

---

## 1. Introduction

Emulsions are constituted of two immiscible liquid phases of which one is dispersed in the form of drops. Mayonnaise, the food emulsion investigated in this work, is made of a continuous aqueous phase and a disperse phase with high content of oil. The stability of the dispersion is provided by molecules present in the egg yolk that act as surfactants and accumulate at the oil-water interface preventing the coalescence of the oil droplets. The droplet size distribution (DSD) is the most important property of the emulsion since it determines the structure, stability, taste, and color of the final product (McClements, 2005). The DSD in turn depends on the composition of the system, the type of process and the operating conditions in which the production process operates (Walstra, 1993). In general, the production of emulsions is based on mixing the ingredients and applying enough mechanical energy to reach the desired DSD. In the case of mayonnaise, this is accomplished by first mixing the ingredients (mainly egg yolk, vinegar, oil, water) in large stirred vessels at moderate rotational speed, and subsequently feeding such premixed emulsion into a high-shear device. Several high-shear devices are used in the process industry (Icardi et al., 2011; Lince et al., 2011; Marchisio et al., 2008) and for emulsions a popular option is the cone mill mixer, where the oil droplets undergo breakage until the final DSD is reached. This last step is crucial to fine-tune the DSD, in order to determine the properties of the final product.

---

\*Corresponding author

 [gianluca.boccardo@polito.it](mailto:gianluca.boccardo@polito.it) (G. Boccardo)

ORCID(s):

16 A typical cone mill mixer is constituted of a solid conical frustum rotor inside a slightly larger stator of the same  
17 shape, forming a small gap in which the emulsion flows and experiences high shear stresses, due to the high rotational  
18 speed of the rotor. The emulsion, before transiting through the high-shear region, flows into a pre-mixing chamber,  
19 followed by a post-mixing chamber.

20 Over time several attempts to model the DSD of mayonnaise have been made (Almeida-Rivera and Bongers, 2010;  
21 Dubbelboer, 2016; Dubbelboer et al., 2016; Maindarkar et al., 2014; Wieringa et al., 1996), but there are still many  
22 issues that need to be completely understood. For example, in the range of shear stresses developed inside the cone  
23 mill, highly concentrated emulsions show non-Newtonian dynamics, depending on both the oil content and the DSD,  
24 that need to be accounted for (Barnes, 1994; Dubbelboer, 2016). In addition, when processing very viscous liquids  
25 the cone mill operates in the laminar regime; however, a simple Poiseuille-Couette flow field can undergo a transition  
26 to the Taylor-Couette regime above a critical operating condition (Li et al., 2010, 2014; Noui-Mehidi et al., 2005;  
27 Wimmer, 2000; Wimmer and Zierep, 2000), where counter-rotating toroidal vortices (also known as Taylor vortices)  
28 appear. Since the transition to Taylor vortices depends strongly on the geometry of the system (Wimmer, 2000) and the  
29 contribution of the axial flow component that has a stabilizing effect on the formation of these instabilities (Giordano  
30 et al., 1998), a detailed flow field analysis must be carried out in order to predict the occurrence of these peculiar flow  
31 patterns. Previous modelling efforts focused on the high-shear zone in the cone mill, while the role of the pre- and  
32 post-mixing zones, before and after the high-shear region, was not investigated. Moreover, the influence of the local  
33 type of flow on drops breakage, namely pure-shear versus elongational, is not clear.

34 Here, we aim to model this last step of the mayonnaise production process in a cone mill by means of 2D and 3D  
35 computational fluid dynamics (CFD) simulations and population balance modelling (PBM) in order to: (1) properly  
36 describe the non-Newtonian dynamics of the emulsion, (2) investigate the role of the pre- and post-mixing zones and  
37 (3) clarify the importance of the local type of flow. In particular, although mayonnaise consists of two distinct phases,  
38 high internal phase emulsions can be considered as a shear-thinning pseudo-single phase system with an apparent  
39 density and viscosity. The apparent emulsion viscosity, as a function of oil content, was evaluated through fitting  
40 of experimental data, by using a power law model with a plateau at the high shear rate end (Dubbelboer, 2016).  
41 In order to describe the evolution of the DSD, the Population Balance Equation (PBE) is employed, in which the  
42 coalescence and breakage of the oil droplets are taken into account by appropriate kernels, which in turn depend on  
43 the local flow conditions, which range from rotation to pure-shear and finally to elongation, depending on the relative  
44 contribution of rotation and strain. Previous PBM were not capable of providing accurate predictions due to their  
45 restrictive assumptions, since coalescence was neglected (Almeida-Rivera and Bongers, 2010; Wieringa et al., 1996).  
46 In fact, although cone mills are designed to promote drop breakage, colliding droplets may coalesce under certain  
47 conditions (Maindarkar et al., 2014, 2012). The Quadrature Method of Moments (QMOM) (Marchisio and Fox, 2013;

48 Marchisio et al., 2003a,b; Mazzei et al., 2012; McGraw, 1997; Sierra-Pallares et al., 2012) is used in order to solve the  
 49 PBE, whereas CFD simulations are performed with the open source CFD code OpenFOAM (version 6.0) (Buffo et al.,  
 50 2016b; Passalacqua et al., 2018).

51 This paper is organized as follows: Section 2 summarizes the main equations used to describe the flow field and the  
 52 DSD evolution, Section 3 reports the details about the simulation test cases and their implementation into OpenFOAM,  
 53 Section 4 focuses on the most important results obtained, and finally Section 5 presents the main conclusions of this  
 54 work.

## 55 2. Theoretical background

56 The emulsification within the rotor-stator system investigated in this work is a steady-state process. Therefore, the  
 57 well-known momentum balance equation for an incompressible, non-Newtonian, and stationary flow is solved in order  
 58 to obtain the flow field (Bird et al., 1960). In this geometry, the centrifugal force that acts on the rotating fluid is not  
 59 perpendicular to the surfaces of the rotor and stator. The flow field between two coaxial conical cylinders can present  
 60 instabilities, known as Taylor vortices (Wimmer, 2000). These vortices are superimposed to the main Couette flow  
 61 with an axial throughput (Giordano et al., 1998). For such particular system, very different flow patterns can develop  
 62 inside the cone mill with varying operating conditions (Noui-Mehidi et al., 2005); however, as it will be shown in  
 63 Section 4, the conditions investigated in this work only result in the appearance of laminar Taylor vortices. Therefore,  
 64 the implementation of a turbulence model is not necessary.

65 In order to evaluate this particular flow pattern, the Reynolds number is calculated as follows:

$$\text{Re} = \frac{\omega R_{max} d}{\nu_{emul}}, \quad (1)$$

66 where  $\omega$  is the angular velocity of the rotor and  $d$  is the distance (gap) between the rotor and the stator. In general, the  
 67 Reynolds number for the investigated system is not constant, since the rotor radius increases from the top to the bottom  
 68 of the cone mill and the viscosity changes locally as a function of the local shear rate  $\dot{\gamma}$ . Therefore, the maximum rotor  
 69 radius  $R_{max}$  and the volume-averaged kinematic apparent viscosity of the emulsion  $\nu_{emul}$  are used in Equation (1). This  
 70 corresponds to the definition used in previous simulation works with whose results we compared our work. For specific  
 71 operating conditions, it is a good approximation to only consider the volume average of the emulsion viscosity  $\bar{\nu}_{emul}$ ,  
 72 since the local shear rate inside the gap section of the cone mill mostly depends on the tangential velocity gradient.  
 73 As it will be shown in Section 4, the tangential component of velocity shows a linear profile (and a constant gradient)  
 74 along the gap width for a specific rotor radius. On the other hand, along the height of the cone mill there are just small

75 variations of the tangential velocity gradient, since the difference between the maximum and the minimum rotor radius  
76 is small (see Figure 2).

## 77 2.1. Non-Newtonian rheology model

78 In order to properly describe the non-Newtonian dynamics of the emulsion, the fluid is considered as a shear-  
79 thinning pseudo-single phase system, with an apparent emulsion viscosity  $\eta_{emul}$  evaluated through a power law model  
80 with a plateau at high shear rates fitted with experiments and reasonably accurate in the range of the local shear rate  $\dot{\gamma}$   
81 developed inside the cone mill mixer ( $10^3 - 10^5 s^{-1}$ ) (Dubbelboer, 2016; Dubbelboer et al., 2016):

$$\frac{\eta_{emul}}{\eta_c} = \eta_r = \eta_{r,\infty} + K\dot{\gamma}^m. \quad (2)$$

82 In Eq. (2),  $\eta_r$  is the dimensionless relative viscosity, expressed as the ratio of apparent emulsion viscosity  $\eta_{emul}$  to  
83 continuous water phase viscosity  $\eta_c$ . The continuous phase consists of egg yolk, salt, and vinegar dissolved in water  
84 and its viscosity was measured to be Newtonian over the range of shear rates investigated and equal to  $10 \text{ mPa} \cdot \text{s}$   
85 (Dubbelboer, 2016; Dubbelboer et al., 2016). In Eq. (2),  $\eta_{r,\infty}$  is the relative plateau viscosity for high shear rates.  
86 The parameters  $\eta_{r,\infty}$ ,  $K$ , and  $m$  result from experimental data fitting and they only depend on the oil concentration  
87 (Dubbelboer, 2016). The kinematic apparent emulsion viscosity is  $\nu_{emul} = \eta_{emul} / \rho_{emul}$ , where  $\rho_{emul}$  is the apparent  
88 emulsion density, calculated as  $\rho_{emul} = \rho_{oil}\phi_v / \phi_w$ . Here,  $\phi_v$  and  $\phi_w$  are respectively the oil volume and the oil weight  
89 fractions, as reported in the reference experimental work (Dubbelboer, 2016; Dubbelboer et al., 2016). It is important  
90 to point out here that Dubbelboer (2016); Dubbelboer et al. (2016) provided a relationship for the apparent emulsion  
91 viscosity as a function of the mean oil droplet diameter in order to link the evolution of the DSD with the macroscopic  
92 rheological properties. However, in this work the approach described in Eq. (2) is employed to describe the non-  
93 Newtonian dynamics of the emulsion for sake of computational simplicity (see Section 3).

## 94 2.2. CFD and PBM description

95 As mentioned, the flow field of the liquid-liquid emulsion in the cone mill is described by solving the steady-  
96 state continuity and momentum balance equations for an incompressible pseudo-single phase non-Newtonian flow, as  
97 detailed in previous works (Boccardo et al., 2014; Tosco et al., 2013). By solving these equations the emulsion velocity  
98 in the cone mill,  $\mathbf{U}$ , described as a pseudo-single phase fluid, is calculated. Numerous interesting flow features can be  
99 extracted via this variable. For example, the local shear rate is calculated as follows:

$$\dot{\gamma} = 2\sqrt{II_E}, \quad (3)$$

100 where  $II_{\mathbf{E}}$  is the second invariant of the symmetric rate-of-strain tensor  $\mathbf{E}$ , which is in turn defined as:

$$\mathbf{E} = \frac{1}{2} [\nabla\mathbf{U} + (\nabla\mathbf{U})^T]. \quad (4)$$

101 Another interesting flow feature is the so-called Manas-Zloczower mixing index, defined as follows:

$$\alpha = \frac{\sqrt{II_{\mathbf{E}}}}{\sqrt{II_{\mathbf{E}}} + \sqrt{II_{\mathbf{\Omega}}}}, \quad (5)$$

102 where  $II_{\mathbf{\Omega}}$  is the second invariant of the skew-symmetric rate-of-rotation tensor  $\mathbf{\Omega}$ , which in turn is defined as:

$$\mathbf{\Omega} = \frac{1}{2} [\nabla\mathbf{U} - (\nabla\mathbf{U})^T]. \quad (6)$$

103 The mixing index  $\alpha$  has a 0-1 range, with 0 indicating a rotational motion, and 0.5 and 1 indicating pure shear and pure  
104 elongational flows, respectively. As we will see both  $\dot{\gamma}$  and  $\alpha$  play an important role during droplet breakup.

105 The evolution of the droplet size distribution (DSD) is properly described by the PBE, accounting for the birth and  
106 death of droplets due to coalescence and breakage. Assuming the emulsification process at steady-state and omitting  
107 explicit indications of space and time dependencies, the PBE can be written as follows (Ramkrishna, 2000):

$$\begin{aligned} \nabla \cdot (\mathbf{U} n(L)) = & \frac{L^2}{2} \int_0^L \frac{C \left( (L^3 - L'^3)^{1/3}, L' \right)}{(L^3 - L'^3)^{2/3}} n \left( (L^3 - L'^3)^{1/3} \right) n(L') dL' \\ & - n(L) \int_0^\infty C(L, L') n(L') dL' + \int_L^\infty g(L') \beta(L|L') n(L') dL' - g(L)n(L), \quad (7) \end{aligned}$$

108 where  $n(L)$  is the DSD (Marchisio and Fox, 2013),  $L$  is the droplet diameter as well as the internal coordinate of the  
109 PBE. The coalescence kernel,  $C(L, L')$ , and the breakage kernel,  $g(L)$ , quantify the rate with which droplets coalesce  
110 and break. The daughter distribution function,  $\beta(L|L')$ , defines instead the size distribution of the droplets formed by  
111 the break-up of a droplet of size  $L'$ .

112 Thanks to the assumption of considering the emulsion as a shear-thinning pseudo-single phase,  $\mathbf{U}$  in Eq. (7) is  
113 the fluid velocity obtained by solving the flow field equation (as explained above). Therefore,  $\mathbf{U}$  represents the first  
114 coupling variable used in this work, and from the flow field it is possible to calculate the local shear rates  $\dot{\gamma}$  (Bird  
115 et al., 1960). The right-hand side of Eq. (7) is the source term due to the coalescence and breakage of the oil droplets,  
116 which are described by means of phenomenological models called kernels (Li et al., 2017). As previously mentioned,  
117 in this work QMOM (Marchisio et al., 2003a,b) is employed to solve the PBM (Equation (7)). The general idea behind  
118 this method is to solve transport equations for the moments of the DSD. By approximating the unknown DSD,  $n(L)$ ,

119 as a summation of Dirac functions and using a quadrature approximation of order  $N$ , QMOM leads to the following  
 120 expression for the moment of order  $k$  (Marchisio et al., 2003b):

$$M_k = \int_0^{+\infty} n(L)L^k dL \approx \sum_{\alpha=1}^N w_{\alpha} L_{\alpha}^k \quad \text{with} \quad k \in 0, \dots, 2N - 1, \quad (8)$$

121 where  $w_{\alpha}$  and  $L_{\alpha}$  are the  $N$  quadrature weights and  $N$  quadrature abscissas, in turn calculated from the first  $2N$  lower-  
 122 order moments through so-called moment inversion algorithms, such as the Product-Difference (PD) (Marchisio and  
 123 Fox, 2013) algorithm employed in this work. The reader can refer to the literature for further details (Boccardo et al.,  
 124 2019; Li et al., 2017; Marchisio and Fox, 2013; Marchisio et al., 2003a,b; McGraw, 1997). Moreover, it is important  
 125 to remark that the moments represent integral properties of the DSD. For example, in the case investigated here,  $M_0$   
 126 represents the number of oil droplets per unit volume, while  $M_3$ , if multiplied by a shape volume coefficient equal  
 127 to  $\pi/6$  due to spherical shape of the droplets, is equal to the oil volume fraction. Most importantly, the mean Sauter  
 128 diameter used in this work for evaluating the evolution of the DSD is simply defined as follows:  $d_{32} = M_3/M_2$ .

129 The coupling between CFD and PBM is realized here by using two approaches. Some of the simulations are run  
 130 with the classical on-the-fly coupling, where the governing equations are solved simultaneously (Gao et al., 2016),  
 131 whereas another part of the simulations is run with the off-line coupling, where first the CFD equations for the flow  
 132 field are solved, the relevant information for the flow field is extracted (i.e. shear rate and mixing index) and finally a  
 133 volume-averaged PBM is solved for the evolution of the DSD (Buffo et al., 2016a; De Bona et al., 2016).

134 Three important functions appear which determine the evolution and the final shape of the DSD: the coalescence  
 135 kernel  $C(L, L')$ , the breakage kernel  $g(L)$  and the daughter-size distribution function  $\beta(L|L')$ . The coalescence  
 136 kernel  $C(L, L')$ , quantifying the rate of coalescence of droplets of diameter  $L$  and  $L'$ , and the breakage kernel  $g(L)$ ,  
 137 quantifying the rate of breakage of droplets of size  $L$ , take respectively the following forms (Maindarkar et al., 2014):

$$C(L, L') = K_1 \frac{\pi}{6} \left( \frac{\dot{\gamma}}{1 - \phi_v} \right) (L + L')^3 \exp \left( -K_2 \lambda \text{Ca}^{\frac{3}{2}} \left( \frac{8\pi\sigma R_{eq}^2}{A_H} \right)^{\frac{1}{3}} \right), \quad (9)$$

$$g(L) = K_3 \dot{\gamma} \exp \left( -K_4 \frac{\text{Ca}_{cr}}{\text{Ca}} \right),$$

138 where  $\phi_v$  is the oil volume fraction,  $A_H$  is the Hamaker constant,  $\lambda$  is the ratio between the oil viscosity  $\eta_{oil}$   
 139 and the apparent emulsion viscosity  $\eta_{emul}$ , and  $K_1$ ,  $K_2$ ,  $K_3$ , and  $K_4$  are free adjustable model parameters to be  
 140 fitted with experimental data.  $R_{eq}$  is the equivalent radius of colliding drops of diameter  $L$  and  $L'$ , defined as:  
 141  $R_{eq} = 2/(2/L + 2/L')$ . Although the interfacial tension  $\sigma$  in Eq. (9) is dynamic for an oil-in-water emulsion as it  
 142 varies according to local flow conditions (Anton, 2013), it is here assumed constant and equal to 10 mN/m as in the

143 work of Dubbelboer et al. (2016). In Eq. (9),  $Ca$  is the capillary number, defined as:

$$Ca = \frac{\eta_{emul} \dot{\gamma} L}{2\sigma}, \quad (10)$$

144 where  $\eta_{emul}$  is the apparent emulsion viscosity and  $\dot{\gamma}$  is the local shear rate.

145 The high shear rates developed inside the mixer tend to stretch the oil droplets and droplet breakage is assumed to  
 146 follow the capillary instability mechanism. This means that, when the ratio of the viscous stress acting on the drops to  
 147 the interfacial tension force, i.e.  $Ca$ , exceeds a critical value, i.e. the critical capillary number  $Ca_{cr}$ , a mother droplet  
 148 breaks into two or more daughter droplets, depending on the form of the daughter-size distribution function  $\beta(L|L')$ .  
 149 The critical capillary number  $Ca_{cr}$  determines the stability of the droplet and depends on the ratio between the viscosity  
 150 of the disperse and continuous phases,  $\lambda$ , and on the type of flow inside a specific geometry (Bentley and Leal, 1986).  
 151 Its expression can usually be derived from experiments and in this work we used two empirical correlations. The first  
 152 one refers to the case of pure shear flow (i.e. mixing index,  $\alpha$ , equal to 0.5) (Debruijn, 1991) as the result of single  
 153 droplet breakup experiments between two concentric cylinders:

$$\log_{10} Ca_{cr} = -0.506 - 0.0994 \log_{10} \lambda + 0.124 (\log_{10} \lambda)^2 - \frac{0.115}{\log_{10} \lambda - 0.611}. \quad (11)$$

154 It is worth mentioning that this expression is valid for  $\lambda < 4$ , as for  $\lambda > 4$  the critical capillary number tends to infinity,  
 155 implying that for  $\lambda > 4$  pure shear flow is not effective in breaking the droplets. The second one refers to the case of  
 156 flows with an elongational component (i.e.  $0.5 < \alpha \leq 1.0$ ) and reads as follows:

$$Ca_{cr} = \frac{0.14 \lambda^{-1/6}}{\alpha^{1/2}}, \quad (12)$$

157 Figure 1 reports the dependency of the critical Capillary number versus the viscosity ratio for two values of the mixing  
 158 index, namely pure shear flow,  $\alpha = 0.5$ , and pure elongational flow  $\alpha = 1.0$ . As it is seen, for every reported value  
 159 of the viscosity ratio  $\lambda$ , the critical Capillary number for pure elongational flow is smaller than for pure shear flow,  
 160 indicating that flows with an elongational component are more effective in breaking droplets. This is particularly true  
 161 for highly viscous disperse phases, where  $\lambda > 4$ . In these cases in fact the critical Capillary number for pure shear  
 162 flows is practically infinitely large, implying that pure shear flow cannot break the droplets, no matter how intense is  
 163 the shear rate. When  $\lambda > 4$  only an elongational component can reduce the drop size.

164 As far as the viscosity ratio,  $\lambda = \eta_d / \eta_c$ , is concerned, this is usually evaluated as the ratio between the disperse and  
 165 continuous phase viscosity. It is however very common, in the case of dense emulsions, to use the apparent emulsion  
 166 viscosity  $\eta_{emul}$  instead of the continuous phase viscosity  $\eta_c$ , as in high disperse phase emulsions, droplets perceive a



167 surrounding continuous phase with the emulsion viscosity (Jansen et al., 2001; Maindarkar et al., 2014). This is also  
 168 consistent with simulating the flow field in the device by using the pseudo-single phase approach.

169 The coalescence kernel  $C(L, L')$  in Eq. (9) is incorporated in the model since colliding drops may coalesce  
 170 despite the cone mill is designed to promote droplet breakage (Maindarkar et al., 2014, 2012). The coalescence rate is  
 171 determined by the product of the frequency of droplet collisions and the probability that a collision event will produce  
 172 coalescence. The collision frequency depends on the local flow field (Klink et al., 2011), and the coalescence probability  
 173 depends on the capillary number  $Ca$  and the viscosity ratio  $\lambda$  (Chesters, 1991). Further details about the expressions of  
 174 kernels used in this work can be found in the literature (Dubbelboer, 2016; Dubbelboer et al., 2016; Maindarkar et al.,  
 175 2014). As it can be seen from Eqs. (9) to (11), the coalescence and the breakage kernels are calculated as functions of  
 176 the local shear rate  $\dot{\gamma}$  and of the local apparent emulsion viscosity  $\eta_{emul}$ , both resulting from solving the flow field.

177 Regarding the daughter-size distribution  $\beta(L|L')$ , it states the size distribution of daughter droplets originating  
 178 from a mother droplet after a breakage event. Here a beta function is employed (Laakkonen et al., 2006):

$$\beta(L, L') = 180 \left( \frac{L^2}{L'^3} \right) \left( \frac{L^3}{L'^3} \right)^2 \left( 1 - \frac{L^3}{L'^3} \right)^2, \quad (13)$$

179 where  $L$  and  $L'$  are the sizes of the daughter and mother droplets. Equation (13) assumes that two droplets are formed  
 180 from a mother and that symmetric breakage is the most likely event. It is important to remind here that the choice of the  
 181 daughter-size distribution function has a large impact on the final DSD (Dubbelboer, 2016; Dubbelboer et al., 2016;  
 182 Maindarkar et al., 2014), but much less on the mean Sauter diameter (Gao et al., 2016), used to evaluate the evolution  
 183 of the DSD in this work. Therefore, the form of the daughter-size distribution function is of secondary importance  
 184 here.

### 185 3. Numerical details

186 As already mentioned, we simulated the last step of the mayonnaise production process, i.e., the cone mill mixer,  
 187 by using CFD and PBM as described in Section 2. The information about the experiments is taken from the work of  
 188 Dubbelboer (2016); Dubbelboer et al. (2016). More in detail, three types of mayonnaise were prepared with different  
 189 concentrations of soybean oil (0.65, 0.70, 0.75 kg/kg), whose density  $\rho_d$  and viscosity  $\eta_d$  are respectively equal to 917  
 190 kg/m<sup>3</sup> and 50 mPa · s (Maindarkar et al., 2014). Before pumping it into the cone mill, the mayonnaise is characterized  
 191 by a coarse DSD, whose shape only depends on the initial oil content. After the continuous mixing process into the  
 192 cone mill, the desired product structure is obtained, i.e. the final DSD is reached. Upstream and downstream DSD  
 193 measurements are available in the literature for model validation.

194 Each one of these three types of mayonnaise was processed under the three different operating conditions reported in  
195 Table 1. The last column reports the corresponding Reynolds numbers for the intermediate soybean oil concentration  
196 (0.70 kg/kg). As it can be seen, only for experiment 1 the Reynolds number exceeds the critical Reynolds number  
197 (also corresponding to the highest Taylor number), highlighting for this operating condition the presence of Taylor  
198 vortices (Li et al., 2010, 2014) (see Section 4.1).

199 A sketch of the cone mill mixer, together with its 2D and 3D representations, is reported in Figure 2. It consists of a  
200 solid conical frustum rotor, which rotates clockwise inside a slightly larger stator of the same shape. This configuration  
201 forms a small gap in which the emulsion flows from the top to the bottom of the cone mill. The chambers before and after  
202 the small gap ensure a homogeneous composition of the emulsion but their role on determining the final DSD is not fully  
203 clear (Dubbelboer, 2016; Dubbelboer et al., 2016). This is why we considered different geometries for the simulations,  
204 including 2D and 3D representations of the gap region, with and without the pre- and post-mixing chambers. Finally, it  
205 is worth mentioning that the pilot scale apparatus (manufactured by IKA) employed in experimental measurements has  
206 a more complex geometry, but the representation reported in Fig. 2 is a reasonable compromise between computational  
207 costs and accuracy (Dubbelboer, 2016).

208 All the simulations were performed with the open source CFD software OpenFOAM (version 6.0). In order to  
209 evaluate the flow field, the SRFSimpleFoam solver is employed, which is a steady-state solver for incompressible  
210 flows in a single rotating frame. This solver adopts the SIMPLE algorithm for the solution of velocity and pressure  
211 coupling. The viscosity model of the emulsion described in Section 2.1 is implemented as an add-on library.

212 In order to properly describe the flow field in the cone mill a grid independence study has been conducted. The six  
213 different grids described in Table 2 were tested. These six grids refer to the 2D geometry limited to the gap, without  
214 pre- and post-mixing chambers. The Table reports the grid resolution along the axial and radial directions, the total  
215 number of cells, the resulting number of Taylor vortices and the volume-averaged shear rate. Only the fine resolution  
216 of Grids 4, 5 and 6 makes it possible to properly describe the flow field, both in terms of the number of Taylor vortices  
217 and volume-averaged shear rate. A similar information is reported in Fig. 3 where a contour plot of the shear rate is  
218 reported for Experiment 3 for Grid 1 and Grid 4. As it is seen the vortex structured emerges and is correctly described  
219 only at the second grid resolution. All subsequent results refer to a grid resolution of at least  $25 \times 360$  cells in the gap.

220 The PBM is solved by means of the QMOM with a three node quadrature, meaning that the first six moments  
221 of the DSD are transported. Although in general the evolution of the DSD has an effect on the emulsion viscosity  
222 (Barnes, 1994), the rheology model here implemented depends only on the disperse phase volume fraction and not on  
223 the oil droplets size. Therefore the hydrodynamics of the emulsion does not depend on the DSD (see Section 2.1). As a  
224 consequence, in all simulations at first only the governing equations of SRFSimpleFoam are solved, in order to obtain  
225 a steady-state flow field information. Then, the variables linking CFD and PBM together, i.e. viscosity and velocity

226 fields (see Section 2.2), are transferred to the PBM model. As mentioned, in this work two approaches are used; for a  
227 limited number of cases the viscosity and velocity field are transferred to the modified scalarTransportFoam in order to  
228 solve the PBM, within the CFD code but assuming the flow field was frozen. Further details about this implementation  
229 can be found in our previous works (Boccardo et al., 2019; Buffo et al., 2013, 2016b; Passalacqua et al., 2018). Here,  
230 the six moments are considered as scalars and their transport equations are incorporated in the scalarTransportFoam  
231 module of OpenFOAM that provides a solver for steady or transient transport equation for a single passive scalar,  
232 obtaining a modified solver for the solution of the six equations simultaneously. The coalescence and breakage kernels  
233 described in Section 2.2 are used to evaluate the droplet coalescence and breakage rates. Alternatively, the shear rate,  
234  $\dot{\gamma}$ , and the mixing index,  $\alpha$ , within the cone mill are extracted and the PBM is solved in a simplified form as described  
235 in previous works (De Bona et al., 2016).

236 An overview of the numerical schemes and of the boundary conditions used in this work can be found in Table  
237 3. Regarding inlet boundary conditions, the zero gradient condition is set for the pressure, whereas for the velocity a  
238 inlet constant profile is imposed, whose value is calculated from the inlet mass flow rate corresponding to experiments  
239 reported in Table 1. The values of inlet moments (and consequentially the inlet  $d_{32}$  value) are calculated from the  
240 experimentally measured inlet DSD.

## 241 4. Results and discussion

242 In this section, the most significant results of the simulations performed will be presented. First, the flow field of  
243 the emulsion inside the mixer is shown, then, results of the PBM simulations are also discussed and compared with  
244 experimental data.

### 245 4.1. Flow field results

246 It is interesting to compare the CFD results obtained with the 2D and 3D geometries with the pre- and post-mixing  
247 chambers. Figure 4 reports this comparison in terms of the axial velocity across the gap for three different axial positions  
248 (inlet, center and outlet) for one operating condition, namely experiment no. 1 of Tab. 1. As it is seen, no significant  
249 difference is observed between the 2D and the 3D predictions, probably due to the intrinsic axialsymmetry of the cone  
250 mill. For this reason from now on only 2D results will be presented and discussed. The streaklines for one operating  
251 condition are reported in Fig. 5. As it is seen two large recirculation zones are identified in the pre- and post-mixing  
252 chambers.

253 As expected, the CFD simulations show a high velocity gradient due to the high rotational speed, in particular the  
254 highest velocity corresponds to the tip velocity of the rotor, as it can be seen in Fig. 6, which shows the contour plot of

255 the velocity magnitude in a magnified longitudinal section of the cone mill with oil concentration equal to 0.70 kg/kg  
 256 (70 wt%) and at operating conditions corresponding to experiment no. 1.

257 Since the rotational speed of the rotor is considerably higher than the inlet fluid velocity, the tangential component  
 258 of velocity is larger than the axial and radial one and the contour plot of the tangential velocity is very similar to the  
 259 one reported in Fig. 6. Moreover, the contour plot shows that the tangential velocity has a linear profile along the gap,  
 260 with the maximum value at the rotor wall and the minimum one at the stator wall, like in a Couette flow.

261 Although the main velocity component is the tangential one, it is more interesting to observe the trend of the axial  
 262 component of the emulsion velocity ( $z$ -component). Figure 7 reports the axial velocity profiles versus the normalized  
 263 distance from the rotor wall at half height of the cone mill, with oil concentration equal to 0.70 kg/kg (70 wt%), and for  
 264 different operating conditions (see Table 1). In experiments no. 2 and 3 the axial velocity presents a parabolic profile,  
 265 in which the maximum value depends on the inlet flow rate. It is worth reminding here that the fluid flow enters where  
 266 the cone mill has the smaller radius (top) and exits where it has the larger one (bottom) (see Figure 2), explaining the  
 267 reason of the negative values of velocity. Experiment no. 1 presents a different shape of the axial velocity. Close to the  
 268 rotor wall, the axial velocity points downward, while its direction is opposite close to the stator wall. Therefore, the  
 269 presence of such backflow suggests that a large vortex appears for this operating condition, extending over the entire  
 270 height of the cone mill. This situation has already been observed in previous works, performed with null axial flow  
 271 (Li et al., 2010, 2014). For a better understanding of the fluid flow, Reynolds numbers (defined in Equation (1)) are  
 272 calculated for the same conditions of the Figure 7 and the results are summarized in Table 1. For experiment no. 1 Re  
 273 is higher than  $Re_c$  (equal to 132 (Noui-Mehidi et al., 2005)), at which value the flow starts to become unstable and  
 274 the first large Taylor vortex appears. Although it has been shown experimentally that the axial flow has a stabilizing  
 275 effect on the formation of instabilities, increasing the value of  $Re_c$  (Giordano et al., 1998), Reynolds numbers (and,  
 276 correspondingly, Taylor numbers) shown in Table 1, for experiment no. 1, is high enough to justify the axial velocity  
 277 trends shown in Figure 7 and to imply the presence of a large vortex filling the entire height of the cone mill.

278 At last it is interesting to discuss the predictions for the shear rate, the mixing index and the corresponding Capillary  
 279 number. Figure 8 reports the contour plots for the ratio between the Capillary number and the critical Capillary number,  
 280 calculated by using the emulsion viscosity and the viscosity of the continuous phase, as well as the mixing index for  
 281 experiments no. 1 and 3. Closer observation of Fig. 8 highlights that most of the breakage occurs in the gap, where  
 282 the Capillary number is larger than its critical value, due to pure shear, namely  $\alpha \approx 0.5$ . Larger values of the mixing  
 283 index, namely  $\alpha \approx 1$ , are observed in the pre- and post-mixing chambers, where however the shear rate is not large  
 284 enough to ensure a value of the Capillary number greater than its critical value. This is also confirmed by the results  
 285 reported in Fig. 9, where the volume distribution of shear rate and mixing index across the cone mill are reported for  
 286 the three investigated operating conditions. As it is seen the highest shear rates ( $\gamma \geq 10^3$  1/s) are observed in regions

287 characterized by mixing index approximately equal to 0.5. We can therefore conclude that, although elongational flow,  
288 generally more effective in breaking droplets, is observed in the pre- and post-mixing chambers, most of the droplet  
289 breakup occurs within the cone mill gap due to pure shear.

## 290 4.2. PBM results

291 As already mentioned, the high rotational speed of the cone mill mixer develops a high-shear rate inside a narrow  
292 gap, in order to obtain the final product with the desired features.

293 Figure 10 reports the trend of the number of the oil droplets per unit volume, corresponding to the moment of  
294 order zero of the DSD, and the oil volume fraction, proportional to the moment of order three of the DSD, along the  
295 normalized distance from the middle point of inlet to the middle point of outlet of the cone mill mixer for different  
296 oil concentrations. Since the oil concentration does not change due to droplet coalescence and breakage, the third-  
297 order moment, which is proportional to the oil volume fraction, remains constant along the gap and is equal to the  
298 corresponding values of different types of mayonnaise, as reported in a previous work (Dubbelboer et al., 2016). On  
299 the other hand, the number of oil droplets per unit volume (the moment of order zero) increases, meaning that droplets  
300 break moving through the mixer, since the total oil amount is constant. In addition, it is important to note that the oil  
301 droplets number is larger for higher oil concentrations.

302 The evolution of the DSD is reported in terms of the mean Sauter diameter  $d_{32}$ , calculated as the ratio between the  
303 third and second-order moments. Thanks to the link between PBM and CFD, as described in Section 2.2, it is possible  
304 to highlight the influence of the flow field, and in particular the high shear rates and the axial velocity, on the trend of  
305  $d_{32}$ . Figure 11 reports the contour plot of  $d_{32}$  along a longitudinal section of the cone mill with oil concentration equal  
306 to 0.70 kg/kg (70 wt%) for the experiments n. 1 and 3. As it can be seen,  $d_{32}$  decreases along the flow direction, since  
307 droplets undergo breakage induced by the high shear rates inside the mixer. These trends exactly reproduce what it  
308 is expected from experimental observations (Dubbelboer, 2016; Dubbelboer et al., 2016). The insets in Figure 11 are  
309 magnified sections of the cone mill that show in detail how the flow field, and in particular the axial velocity, influences  
310  $d_{32}$  trends. For experiment n. 3, the  $d_{32}$  presents a parabolic profile along the gap width, with the higher value at the  
311 center of the gap and the lower at the walls, similarly to the respective axial component of velocity (see Figure 7). For  
312 experiment n. 1, the situation is different from experiment n. 3. In this case, it is represented very clearly how the flow  
313 field can influence the local DSD. As it is reported in Section 4.1 and Figure 7, the presence of Taylor instability inside  
314 the mixer leads to a particular shape of velocity profile. Therefore, the link between CFD and PBM is able to show that  
315 the oil droplets are bigger close to the rotor and smaller close to the stator. The average outlet values of  $d_{32}$  shown in  
316 Figure 11 are equal to 7.1  $\mu\text{m}$  for case no. 3 and 5.4  $\mu\text{m}$  for case no. 1, whereas the experimental ones are respectively  
317 7.7  $\mu\text{m}$  and 6.6  $\mu\text{m}$  (Dubbelboer et al., 2016), with a relative error under 20%. This outcomes are obtained by suitably

318 adjusting the free parameters that appear in coalescence and breakage kernels, through a trial and error procedure and  
319 more details on this are given below. It is important to point out that the results reported here have illustrative purposes,  
320 to show the capabilities of the CFD-PBM approach. Achieving a unique and generic set of the free parameters that  
321 matches all the experimental data, using optimization and uncertainty quantification techniques, will be the scope of  
322 future works.

323 As just mentioned the predictions of the PBM are highly affected by the values of the model parameters appearing  
324 in the coalescence kernel,  $K_1$  and  $K_2$ , and the breakage kernel,  $K_3$  and  $K_4$ . Due to the semi-empirical nature of these  
325 kernels and the many approximations adopted in their derivation, their values cannot be predicted by the theory but  
326 have to be fitted with experiments. An example of the influence of the model parameters on the final predictions can be  
327 found in Table 4. As expected by increasing  $K_1$  coalescence becomes more important and the mean Sauter diameter  
328 increases, and conversely by increasing  $K_3$  or  $K_4$  breakup becomes more important and the mean Sauter diameter  
329 decreases.

330 In order to optimize the model parameters  $K_1$ ,  $K_2$ ,  $K_3$  and  $K_4$  the PBM, solved in the simplified form described in  
331 our previous work (De Bona et al., 2016), has been coupled with the covariance matrix adaptation evolution strategy  
332 (CMA-ES) algorithm (Hansen, 2006). The algorithm minimized the normalized distance between the predicted mean  
333 Sauter diameter and the corresponding experimental values, resulting in the final predictions reported in Table 5. The  
334 optimization was performed with the PBM implemented in its simplified form, rather than with the full CFD-PBM  
335 due to the computational costs associated with the full CFD-PBM which are prohibitive for these applications. As it  
336 can be seen from Table 5 the comparison is satisfactory as the PBM is capable of capturing the most important trends  
337 for the investigated operating conditions.

## 338 5. Conclusions

339 In this work we presented a modelling approach for the food emulsion production in a high-shear mixer. A flow  
340 field analysis performed with CFD shows that recognizable patterns for the investigated geometry are in agreement  
341 with previous experimental works. In particular, the tangential component of the emulsion velocity shows a Couette  
342 flow, whereas the axial velocity trends depend on Reynolds number: for  $Re < Re_c$ , a Poiseuille flow develops inside  
343 the gap of the mixer, but above  $Re_c$  the first instability appears and backflow occurs. Thanks to the coupling between  
344 CFD and PBM, demonstrated with two approaches, it is possible to obtain a better understanding of the flow influence  
345 on the evolution of the droplet size distribution. In particular the role of the type of flow, elongational versus pure  
346 shear, and the role of the pre- and post-mixing chambers in the cone mill have been elucidated. This model accounts  
347 for both the coalescence and the breakage of the oil droplets, which depend in turn on the local flow conditions. From  
348 the evaluation of the mean oil droplet diameter, the simulations are able to show that the breaking of the oil droplets

349 promoted by the high shear rates prevails over the coalescence phenomenon, reproducing correctly the experimental  
350 data. As a powerful and convenient method for such kind of applications, QMOM is employed for the solution of the  
351 population balance equation, taking into account the actual hydrodynamics of the emulsion in order to provide a more  
352 accurate prediction of the droplet size distribution.

353 The results presented here will also serve as the basis for future extension of this work in several directions. First, an  
354 optimization procedure will be employed in order to identify an accurate and generic set of kernel constants reproducing  
355 the available experimental data. Then, these simulations can be included in a more general multi-scale framework in  
356 which the effect of the DSD on the emulsion viscosity can be taken into account via detailed front-tracking simulations,  
357 and the interfacial tension can be directly computed with the help of atomistic techniques, such as molecular dynamics  
358 or dissipative particle dynamics.

## 359 **Acknowledgments**

## 360 **Financial disclosure**

361 This work was carried out in the context of the VIMMP project ([www.vimmp.eu](http://www.vimmp.eu)), where the entire workflow will  
362 contribute to populate a marketplace for generic multiscale and multiphysics simulations. The VIMMP project has  
363 received funding from the European Union's Horizon 2020 Research Innovation Programme under Grant Agreement  
364 n. 760907.

## 365 **Conflict of interest**

366 The authors declare no potential conflict of interests.

## 367 **References**

- 368 Almeida-Rivera, C., Bongers, P., 2010. Modelling and experimental validation of emulsification processes in continuous rotor–stator units. *Com-*  
369 *puters & Chemical Engineering* 34, 592 – 597. URL: <http://www.sciencedirect.com/science/article/pii/S009813541000030X>,  
370 doi:<https://doi.org/10.1016/j.compchemeng.2010.01.017>.
- 371 Anton, M., 2013. Egg yolk: structures, functionalities and processes. *Journal of the Science of Food and Agriculture*  
372 93, 2871–2880. URL: <https://onlinelibrary.wiley.com/doi/abs/10.1002/jsfa.6247>, doi:10.1002/jsfa.6247,  
373 arXiv:<https://onlinelibrary.wiley.com/doi/pdf/10.1002/jsfa.6247>.
- 374 Barnes, H.A., 1994. Rheology of emulsions - a review. *Colloids and Surfaces A: Physicochemical and Engineering Aspects* 91,  
375 89 – 95. URL: <http://www.sciencedirect.com/science/article/pii/092777579302719U>, doi:[https://doi.org/10.1016/0927-7757\(93\)02719-U](https://doi.org/10.1016/0927-7757(93)02719-U).
- 377 Bentley, B.J., Leal, L.G., 1986. An experimental investigation of drop deformation and breakup in steady, two-dimensional linear flows. *Journal of*  
378 *Fluid Mechanics* 167, 241–283. doi:10.1017/S0022112086002811.
- 379 Bird, R.B., Stewart, W.E., Lightfoot, E.N., 1960. *Transport Phenomena*. John Wiley and Sons, Inc., New York.

- 380 Boccardo, G., Marchisio, D.L., Sethi, R., 2014. Microscale simulation of particle deposition in porous media. *Journal of Colloid and Interface*  
381 *Science* 417, 227–237. URL: [https://www.scopus.com/inward/record.uri?eid=2-s2.0-84890195092&doi=10.1016%2fj.jcis.](https://www.scopus.com/inward/record.uri?eid=2-s2.0-84890195092&doi=10.1016%2fj.jcis.2013.11.007&partnerID=40&md5=03bbbe3c6b053866c5e16eadacc5addf)  
382 2013.11.007&partnerID=40&md5=03bbbe3c6b053866c5e16eadacc5addf. cited By 34.
- 383 Boccardo, G., Sethi, R., Marchisio, D.L., 2019. Fine and ultrafine particle deposition in packed-bed catalytic reactors. *Chemical Engineering*  
384 *Science* 198, 290–304.
- 385 Buffo, A., De Bona, J., Vanni, M., Marchisio, D.L., 2016a. Simplified volume-averaged models for liquid–liquid dispersions: Correct derivation and  
386 comparison with other approaches. *Chemical Engineering Science* 153, 382–393. URL: [https://www.scopus.com/inward/record.uri?](https://www.scopus.com/inward/record.uri?eid=2-s2.0-84980383589&doi=10.1016%2fj.ces.2016.07.032&partnerID=40&md5=8aad839e2196433ee64beb32429d50eb,doi:10.1016/j.ces.2016.07.032)  
387 [eid=2-s2.0-84980383589&doi=10.1016%2fj.ces.2016.07.032&partnerID=40&md5=8aad839e2196433ee64beb32429d50eb,](https://www.scopus.com/inward/record.uri?eid=2-s2.0-84980383589&doi=10.1016%2fj.ces.2016.07.032&partnerID=40&md5=8aad839e2196433ee64beb32429d50eb,doi:10.1016/j.ces.2016.07.032)  
388 [doi:10.1016/j.ces.2016.07.032.](https://www.scopus.com/inward/record.uri?eid=2-s2.0-84980383589&doi=10.1016%2fj.ces.2016.07.032&partnerID=40&md5=8aad839e2196433ee64beb32429d50eb,doi:10.1016/j.ces.2016.07.032)
- 389 Buffo, A., Marchisio, D.L., Vanni, M., Renze, P., 2013. Simulation of polydisperse multiphase systems using population balances and example  
390 application to bubbly flows. *Chemical Engineering Research and Design* 91, 1859–1875. URL: [http://www.sciencedirect.com/science/](http://www.sciencedirect.com/science/article/pii/S0263876213002645)  
391 [article/pii/S0263876213002645](http://www.sciencedirect.com/science/article/pii/S0263876213002645), doi:<https://doi.org/10.1016/j.cherd.2013.06.021>.
- 392 Buffo, A., Vanni, M., Marchisio, D.L., 2016b. On the implementation of moment transport equations in OpenFOAM: Boundedness and  
393 realizability. *International Journal of Multiphase Flow* 85, 223–235. URL: [http://www.sciencedirect.com/science/article/pii/](http://www.sciencedirect.com/science/article/pii/S0301932215300525)  
394 [S0301932215300525](http://www.sciencedirect.com/science/article/pii/S0301932215300525), doi:<https://doi.org/10.1016/j.ijmultiphaseflow.2016.06.017>.
- 395 Chesters, A.K., 1991. The modelling of coalescence processes in fluid-liquid dispersions: a review of current understanding. *Chemical Engineering*  
396 *Research and Design* 69, 259–270.
- 397 De Bona, J., Buffo, A., Vanni, M., Marchisio, D.L., 2016. Limitations of simple mass transfer models in polydisperse liquid-liquid dispersions.  
398 *Chemical Engineering Journal* 296, 112–121. URL: [https://www.scopus.com/inward/record.uri?eid=2-s2.0-84962319030&doi=](https://www.scopus.com/inward/record.uri?eid=2-s2.0-84962319030&doi=10.1016%2fj.cej.2016.03.070&partnerID=40&md5=d0591a4797c2ce41fea5c1b8ae4933d3,doi:10.1016/j.cej.2016.03.070)  
399 [10.1016%2fj.cej.2016.03.070&partnerID=40&md5=d0591a4797c2ce41fea5c1b8ae4933d3](https://www.scopus.com/inward/record.uri?eid=2-s2.0-84962319030&doi=10.1016%2fj.cej.2016.03.070&partnerID=40&md5=d0591a4797c2ce41fea5c1b8ae4933d3,doi:10.1016/j.cej.2016.03.070), doi:10.1016/j.cej.2016.03.070.
- 400 Debruijn, R.A., 1991. Deformation and breakup of drops in simple shear flows. Ph.D. thesis. Technische Univ., Eindhoven (Netherlands).
- 401 Dubbelboer, A., 2016. Towards optimization of emulsified consumer products : modeling and optimization of sensory and physicochemical aspects.  
402 Ph.D. thesis. Technische Universiteit Eindhoven. Department of Chemical Engineering and Chemistry.
- 403 Dubbelboer, A., Janssen, J.J.M., Hoogland, H., Zondervan, E., Meuldijk, J., 2016. Pilot-scale production process for high internal phase emulsions:  
404 Experimentation and modeling. *Chemical Engineering Science* 148, 32–43. URL: [http://www.sciencedirect.com/science/article/](http://www.sciencedirect.com/science/article/pii/S0009250916301233)  
405 [pii/S0009250916301233](http://www.sciencedirect.com/science/article/pii/S0009250916301233), doi:<https://doi.org/10.1016/j.ces.2016.03.014>.
- 406 Gao, Z., Li, D., Buffo, A., Podgórska, W., Marchisio, D.L., 2016. Simulation of droplet breakage in turbulent liquid–liquid dispersions with CFD-  
407 PBM: Comparison of breakage kernels. *Chemical Engineering Science* 142, 277 – 288. URL: [http://www.sciencedirect.com/science/](http://www.sciencedirect.com/science/article/pii/S0009250915007642)  
408 [article/pii/S0009250915007642](http://www.sciencedirect.com/science/article/pii/S0009250915007642), doi:<https://doi.org/10.1016/j.ces.2015.11.040>.
- 409 Giordano, R.C., Giordano, R.L.C., Prazeres, D.M.F., Cooney, C.L., 1998. Analysis of a Taylor–Poiseuille vortex flow reactor—I: Flow patterns and  
410 mass transfer characteristics. *Chemical Engineering Science* 53, 3635–3652. URL: [http://www.sciencedirect.com/science/article/](http://www.sciencedirect.com/science/article/pii/S0009250998001791)  
411 [pii/S0009250998001791](http://www.sciencedirect.com/science/article/pii/S0009250998001791), doi:[https://doi.org/10.1016/S0009-2509\(98\)00179-1](https://doi.org/10.1016/S0009-2509(98)00179-1).
- 412 Hansen, N., 2006. *The CMA Evolution Strategy: A Comparing Review*. Springer Berlin Heidelberg, Berlin, Heidelberg. pp. 75–102.
- 413 Icardi, M., Gavi, E., Marchisio, D.L., Olsen, M.G., Fox, R.O., Lakehal, D., 2011. Validation of LES predictions for turbulent flow in a Confined  
414 Impinging Jets Reactor. *Applied Mathematical Modelling* 35, 1591–1602. URL: [https://www.scopus.com/inward/record.uri?eid=](https://www.scopus.com/inward/record.uri?eid=2-s2.0-78650273079&doi=10.1016%2fj.apm.2010.09.035&partnerID=40&md5=207f33f79bb49994da4027060a2d9bb3)  
415 [2-s2.0-78650273079&doi=10.1016%2fj.apm.2010.09.035&partnerID=40&md5=207f33f79bb49994da4027060a2d9bb3](https://www.scopus.com/inward/record.uri?eid=2-s2.0-78650273079&doi=10.1016%2fj.apm.2010.09.035&partnerID=40&md5=207f33f79bb49994da4027060a2d9bb3). cited By  
416 32.



- 417 Jansen, K.M.B., Agterof, W.G.M., Mellema, J., 2001. Droplet breakup in concentrated emulsions. *Journal of Rheology* 45, 227–236. doi:10.1122/  
418 1.1333001.
- 419 Klink, I.M., Phillips, R.J., Dungan, S.R., 2011. Effect of emulsion drop-size distribution upon coalescence in simple shear flow: A population  
420 balance study. *Journal of Colloid and Interface Science* 353, 467–475. URL: [http://www.sciencedirect.com/science/article/pii/  
421 S0021979710011100](http://www.sciencedirect.com/science/article/pii/S0021979710011100), doi:<https://doi.org/10.1016/j.jcis.2010.09.059>.
- 422 Laakkonen, M., Alopaeus, V., Aittamaa, J., 2006. Validation of bubble breakage, coalescence and mass transfer models for gas–liquid dispersion  
423 in agitated vessel. *Chemical Engineering Science* 61, 218 – 228. URL: [http://www.sciencedirect.com/science/article/pii/  
424 S0009250905004550](http://www.sciencedirect.com/science/article/pii/S0009250905004550), doi:<https://doi.org/10.1016/j.ces.2004.11.066>.
- 425 Li, D., Gao, Z., Buffo, A., Podgorska, W., Marchisio, D.L., 2017. Droplet breakage and coalescence in liq-  
426 uid–liquid dispersions: Comparison of different kernels with EQMOM and QMOM. *AIChE Journal* 63, 2293–  
427 2311. URL: <https://aiche.onlinelibrary.wiley.com/doi/abs/10.1002/aic.15557>, doi:10.1002/aic.15557,  
428 arXiv:<https://aiche.onlinelibrary.wiley.com/doi/pdf/10.1002/aic.15557>.
- 429 Li, Q.S., Pu, W., Xu, L.x., 2010. Transition to Taylor vortex flow between rotating conical cylinders. *Journal of Hydrodynamics, Ser. B* 22,  
430 241–245. URL: <http://www.sciencedirect.com/science/article/pii/S1001605809600500>, doi:[https://doi.org/10.1016/  
431 S1001-6058\(09\)60050-0](https://doi.org/10.1016/S1001-6058(09)60050-0).
- 432 Li, X., Zhang, J.j., Xu, L.x., 2014. A numerical investigation of the flow between rotating conical cylinders of two different configurations. *Journal of*  
433 *Hydrodynamics* 26, 431–435. URL: [https://doi.org/10.1016/S1001-6058\(14\)60049-4](https://doi.org/10.1016/S1001-6058(14)60049-4), doi:10.1016/S1001-6058(14)60049-4.
- 434 Lince, F., Marchisio, D.L., Barresi, A.A., 2011. A comparative study for nanoparticle production with passive mixers via solvent-  
435 displacement: Use of CFD models for optimization and design. *Chemical Engineering and Processing: Process Intensification* 50, 356–  
436 368. URL: [https://www.scopus.com/inward/record.uri?eid=2-s2.0-79955107468&doi=10.1016%2fj.cep.2011.02.015&  
437 partnerID=40&md5=0b3bdc1a42303dfda1abc952a540f1aa](https://www.scopus.com/inward/record.uri?eid=2-s2.0-79955107468&doi=10.1016%2fj.cep.2011.02.015&partnerID=40&md5=0b3bdc1a42303dfda1abc952a540f1aa). cited By 36.
- 438 Maindarkar, S., Dubbelboer, A., Meuldijk, J., Hoogland, H., Henson, M., 2014. Prediction of emulsion drop size distributions in colloid mills.  
439 *Chemical Engineering Science* 118, 114–125. URL: <http://www.sciencedirect.com/science/article/pii/S0009250914003777>,  
440 doi:<https://doi.org/10.1016/j.ces.2014.07.032>.
- 441 Maindarkar, S.N., Raikar, N.B., Bongers, P., Henson, M.A., 2012. Incorporating emulsion drop coalescence into population balance equation models  
442 of high pressure homogenization. *Colloids and Surfaces A: Physicochemical and Engineering Aspects* 396, 63 – 73. URL: [http://www.  
443 sciencedirect.com/science/article/pii/S0927775711007874](http://www.sciencedirect.com/science/article/pii/S0927775711007874), doi:<https://doi.org/10.1016/j.colsurfa.2011.12.041>.
- 444 Marchisio, D.L., Fox, R.O., 2013. *Computational Models for Polydisperse Particulate and Multiphase Systems*. Cambridge University Press,  
445 Cambridge. URL: <https://books.google.it/books?id=SyEAy7zx6zIC>.
- 446 Marchisio, D.L., Omegna, F., Barresi, A.A., Bowen, P., 2008. Effect of mixing and other operating parameters in sol-gel processes. *Industrial and*  
447 *Engineering Chemistry Research* 47, 7202–7210. URL: [https://www.scopus.com/inward/record.uri?eid=2-s2.0-54249129441&  
448 doi=10.1021%2fie800217b&partnerID=40&md5=8acd653ef62d97d4bde71a3d47d2f8f2](https://www.scopus.com/inward/record.uri?eid=2-s2.0-54249129441&doi=10.1021%2fie800217b&partnerID=40&md5=8acd653ef62d97d4bde71a3d47d2f8f2). cited By 39.
- 449 Marchisio, D.L., Pikturna, J.T., Fox, R.O., Vigil, R.D., Barresi, A.A., 2003a. Quadrature method of moments for population-balance equations.  
450 *AIChE Journal* 49, 1266–1276. URL: <https://aiche.onlinelibrary.wiley.com/doi/abs/10.1002/aic.690490517>, doi:10.1002/  
451 aic.690490517, arXiv:<https://aiche.onlinelibrary.wiley.com/doi/pdf/10.1002/aic.690490517>.
- 452 Marchisio, D.L., Vigil, R.D., Fox, R.O., 2003b. Quadrature method of moments for aggregation–breakage processes. *Journal of Colloid and*  
453 *Interface Science* 258, 322 – 334. URL: <http://www.sciencedirect.com/science/article/pii/S0021979702000541>, doi:[https://doi.org/10.1016/S0021-9797\(02\)00054-1](https://doi.org/10.1016/S0021-9797(02)00054-1).  
454

- 455 Mazzei, L., Marchisio, D.L., Lettieri, P., 2012. New quadrature-based moment method for the mixing of inert polydisperse fluidized powders in com-  
456 mercial CFD codes. *AIChE Journal* 58, 3054–3069. URL: [https://www.scopus.com/inward/record.uri?eid=2-s2.0-84866047786&](https://www.scopus.com/inward/record.uri?eid=2-s2.0-84866047786&doi=10.1002%2faic.13714&partnerID=40&md5=349b0e4b8d5c838d05e7023773d1de5a)  
457 [doi=10.1002%2faic.13714&partnerID=40&md5=349b0e4b8d5c838d05e7023773d1de5a](https://www.scopus.com/inward/record.uri?eid=2-s2.0-84866047786&doi=10.1002%2faic.13714&partnerID=40&md5=349b0e4b8d5c838d05e7023773d1de5a). cited By 34.
- 458 McClements, D.J., 2005. *Food Emulsions: Principles, Practice, and Techniques*. CRC Press, Boca Raton, FL.
- 459 McGraw, R., 1997. Description of Aerosol Dynamics by the Quadrature Method of Moments. *Aerosol Science and*  
460 *Technology* 27, 255–265. URL: <https://doi.org/10.1080/02786829708965471>, doi:10.1080/02786829708965471,  
461 [arXiv:https://doi.org/10.1080/02786829708965471](https://arxiv.org/abs/10.1080/02786829708965471).
- 462 Noui-Mehidi, M.N., Ohmura, N., Kataoka, K., 2005. Dynamics of the helical flow between rotating conical cylinders. *Journal of Fluids and*  
463 *Structures* 20, 331–344. URL: <http://www.sciencedirect.com/science/article/pii/S0889974605000149>, doi:<https://doi.org/10.1016/j.jfluidstructs.2004.12.001>.
- 464 [org/10.1016/j.jfluidstructs.2004.12.001](https://doi.org/10.1016/j.jfluidstructs.2004.12.001).
- 465 Passalacqua, A., Laurent, F., Madadi-Kandjani, E., Heylmu, J.C., Fox, R.O., 2018. An open-source quadrature-based population balance  
466 solver for OpenFOAM. *Chemical Engineering Science* 176, 306–318. URL: [http://www.sciencedirect.com/science/article/pii/](http://www.sciencedirect.com/science/article/pii/S0009250917306590)  
467 [S0009250917306590](http://www.sciencedirect.com/science/article/pii/S0009250917306590), doi:<https://doi.org/10.1016/j.ces.2017.10.043>.
- 468 Ramkrishna, D., 2000. *Population Balances: Theory and Applications to Particulate Systems in Engineering*. Academic Press, London. URL:  
469 <https://books.google.it/books?id=Ep0N3osDPY4C>.
- 470 Sierra-Pallares, J., Marchisio, D.L., Parra-Santos, M.T., García-Serna, J., Castro, F., Cocero, M.J., 2012. A computational fluid dynamics study of  
471 supercritical antisolvent precipitation: Mixing effects on particle size. *AIChE Journal* 58, 385–398. URL: [https://www.scopus.com/inward/](https://www.scopus.com/inward/record.uri?eid=2-s2.0-80051473422&doi=10.1002%2faic.12594&partnerID=40&md5=4a7a50d5ed1ed62527f2a0404ff458e8)  
472 [record.uri?eid=2-s2.0-80051473422&doi=10.1002%2faic.12594&partnerID=40&md5=4a7a50d5ed1ed62527f2a0404ff458e8](https://www.scopus.com/inward/record.uri?eid=2-s2.0-80051473422&doi=10.1002%2faic.12594&partnerID=40&md5=4a7a50d5ed1ed62527f2a0404ff458e8).  
473 cited By 39.
- 474 Tosco, T., Marchisio, D.L., Lince, F., Sethi, R., 2013. Extension of the Darcy-Forchheimer Law for Shear-Thinning Fluids and Validation  
475 via Pore-Scale Flow Simulations. *Transport in Porous Media* 96, 1–20. URL: [https://www.scopus.com/inward/record.uri?eid=](https://www.scopus.com/inward/record.uri?eid=2-s2.0-84870562743&doi=10.1007%2fs11242-012-0070-5&partnerID=40&md5=0c927007bf22f9e2299c10fc2ddb6f80)  
476 [2-s2.0-84870562743&doi=10.1007%2fs11242-012-0070-5&partnerID=40&md5=0c927007bf22f9e2299c10fc2ddb6f80](https://www.scopus.com/inward/record.uri?eid=2-s2.0-84870562743&doi=10.1007%2fs11242-012-0070-5&partnerID=40&md5=0c927007bf22f9e2299c10fc2ddb6f80), doi:10.  
477 [1007/s11242-012-0070-5](https://www.scopus.com/inward/record.uri?eid=2-s2.0-84870562743&doi=10.1007%2fs11242-012-0070-5&partnerID=40&md5=0c927007bf22f9e2299c10fc2ddb6f80).
- 478 Walstra, P., 1993. Principles of emulsion formation. *Chemical Engineering Science* 48, 333 – 349. URL: [http://www.sciencedirect.com/](http://www.sciencedirect.com/science/article/pii/000925099380021H)  
479 [science/article/pii/000925099380021H](http://www.sciencedirect.com/science/article/pii/000925099380021H), doi:[https://doi.org/10.1016/0009-2509\(93\)80021-H](https://doi.org/10.1016/0009-2509(93)80021-H).
- 480 Wieringa, J.A., Vandieren, F., Janssen, J.J., Agterof, W.G., 1996. Droplet breakup mechanisms during emulsification in colloid mills at high dispersed  
481 phase volume fraction. *Chemical Engineering Research and Design* 74, 554–562. URL: [https://www.scopus.com/inward/record.uri?](https://www.scopus.com/inward/record.uri?eid=2-s2.0-3042948605&partnerID=40&md5=98df383788284438d110eee7171c1f96)  
482 [eid=2-s2.0-3042948605&partnerID=40&md5=98df383788284438d110eee7171c1f96](https://www.scopus.com/inward/record.uri?eid=2-s2.0-3042948605&partnerID=40&md5=98df383788284438d110eee7171c1f96).
- 483 Wimmer, M., 2000. Taylor vortices at different geometries, in: Egbers, C., Pfister, G. (Eds.), *Physics of Rotating Fluids*, Springer Berlin Heidelberg,  
484 Berlin, Heidelberg. pp. 194–212.
- 485 Wimmer, M., Zierep, J., 2000. Transition from Taylor vortices to cross-flow instabilities. *Acta Mechanica* 140, 17–30. URL: <https://doi.org/10.1007/BF01175977>,  
486 [doi:10.1007/BF01175977](https://doi.org/10.1007/BF01175977).

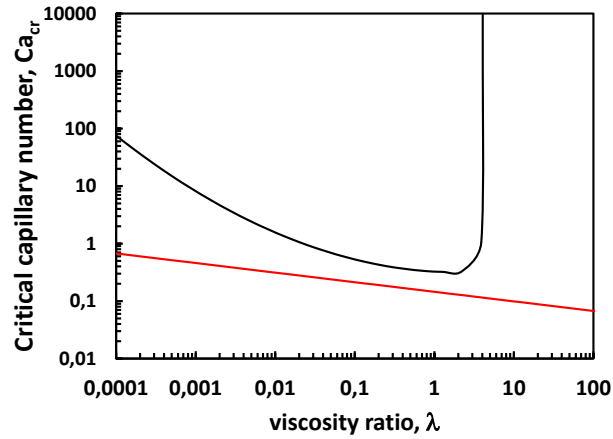


**Figure 1:** Dependency of the critical Capillary number versus the viscosity ratio for pure shear flow (black line  $\alpha = 0.5$ ) and pure elongational flow (red line  $\alpha = 1.0$ ).

**Table 1**

Design of experimental test cases from the work of Dubbelboer (2016); Dubbelboer et al. (2016) and corresponding Reynolds numbers at oil concentration equal to 0.70 kg/kg (70 wt%).

Experiment no.	Rotor speed (rpm)	Gap (mm)	Inlet mass flow rate (kg/h)	Re
1	6039	0.624	31	140.0 > $Re_c$
2	6784	0.208	15	61.2
3	3170	0.624	64	64.6

**Table 2**

Grid independence study on a 2D geometry without pre- and post-mixing chambers for Experiment n. 1 and for a disperse phase concentration of 0.65 kg/kg.

	Grid 1	Grid 2	Grid 3	Grid 4	Grid 5	Grid 6
Number of cells along the radial direction	10	15	20	25	30	35
Number of cells along the axial direction	150	220	285	360	430	500
Total number of cells	1500	3300	5700	9000	12900	17500
Number of Taylor vortices	3	16	19	21	21	21
Volume-averaged shear rate (1/s)	28991	29733	30339	30540	30605	30758

**Table 3**

Numerical schemes and boundary conditions used in the simulations.

Variable	Scheme	Boundary condition			
		Rotor wall	Stator wall	Inlet	Outlet
Pressure	Second-order central scheme	Zero gradient	Zero gradient	Zero gradient	Fixed value
Fluid velocity	Bounded second-order upwind	Rotor speed	No-slip	Constant profile	Zero gradient
Moments	Bounded first-order upwind	Zero gradient	Zero gradient	Fixed value	Zero gradient

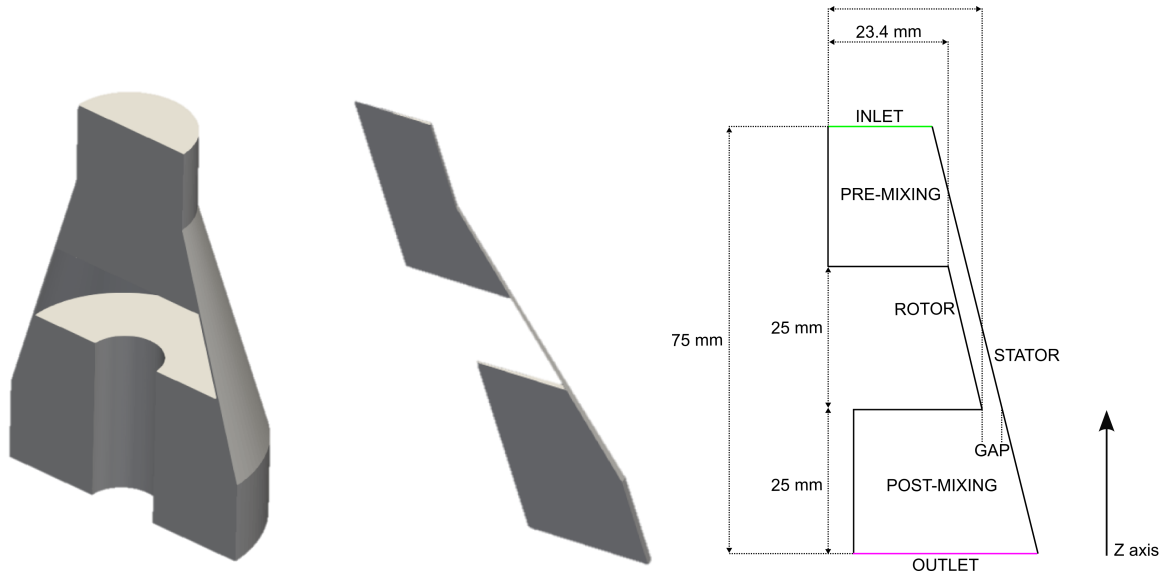


**Figure 2:** Sketch of the cone mill mixer (right) and corresponding 3D (left) and 2D (center) representations.

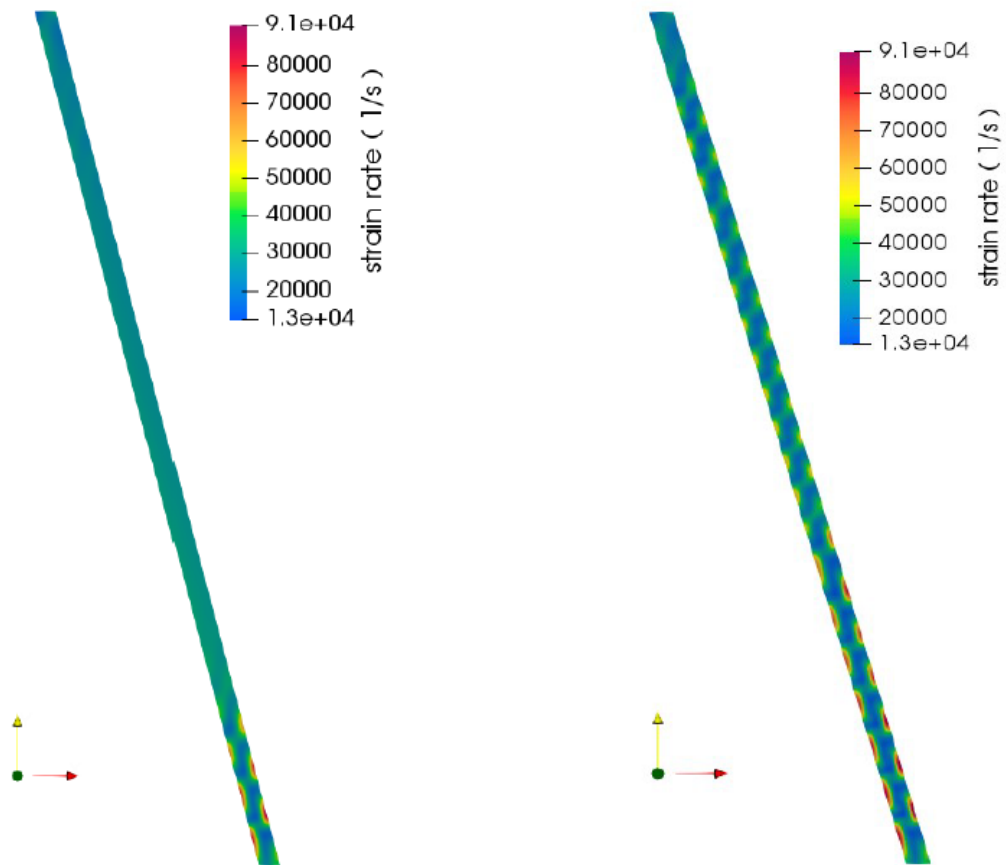


**Figure 3:** Contour plots of the shear rate reported for Experiment 3 for grid 1 (left) and grid 4 (right).

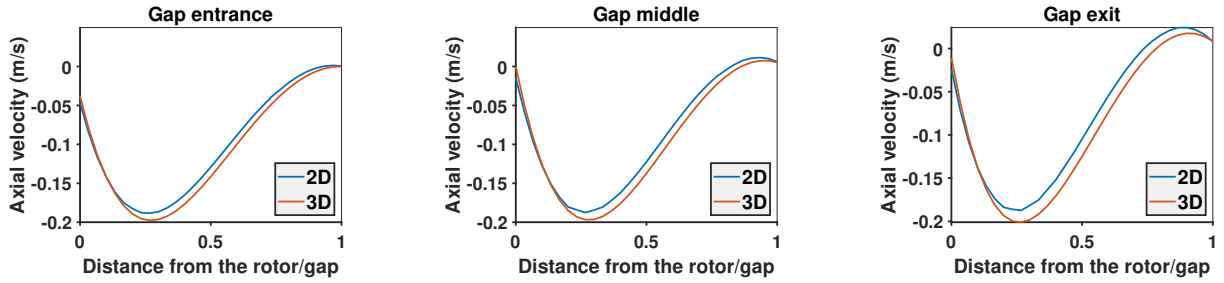


**Figure 4:** Axial velocity across the gap (normalized distance from the rotating wall) at the gap inlet, center and outlet, as predicted by 2D and 3D simulations for experiment no. 1 and for a disperse phase concentration of 0.70 kg/kg.

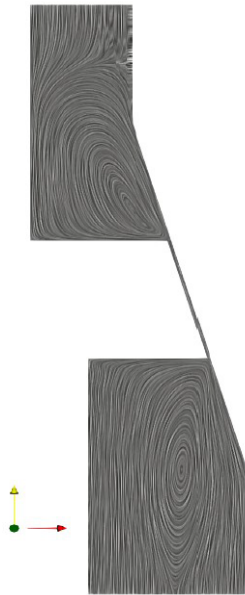


**Figure 5:** Streaklines for experiment no. 1 and for a disperse phase concentration of 0.65 kg/kg

**Table 4**

Comparison between PBM predictions and experimental measurements for the mean Sauter diameter for experiments no. 1 and 3 for different values of the coalescence kernel constants,  $K_1$  and  $K_2$ , and the breakage kernel constants,  $K_3$  and  $K_4$ .

Experiment	$K_1$	$K_2$	$K_3$	$K_4$	$d_{32}^{Model}(\mu\text{m})$	$d_{32}^{Exp}(\mu\text{m})$
no. 1	$1 \times 10^{-6}$	$1.077 \times 10^2$	$2.154 \times 10^{-4}$	$1.744 \times 10^{-3}$	6.9	6.6
	$2.154 \times 10^{-4}$	$1.498 \times 10^{-6}$	$4.642 \times 10^{-2}$	2.684	3.6	
	$1 \times 10^1$	$1.077 \times 10^2$	$2.154 \times 10^{-4}$	2.684	23.7	
no. 3	$1 \times 10^{-6}$	$1.077 \times 10^2$	$2.154 \times 10^{-4}$	$1.744 \times 10^{-3}$	29.1	7.7
	$2.154 \times 10^{-4}$	$1.498 \times 10^{-6}$	$4.642 \times 10^{-2}$	2.684	6.7	
	$1 \times 10^1$	$1.077 \times 10^2$	$2.154 \times 10^{-4}$	2.684	32.0	

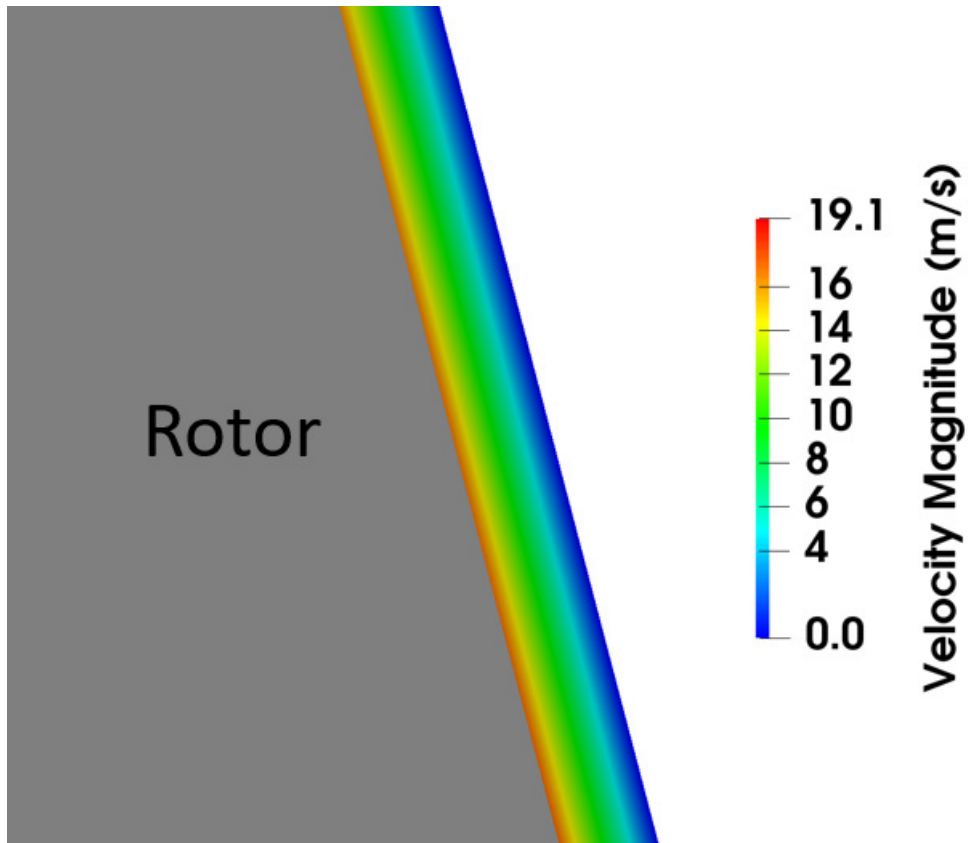


**Figure 6:** Contour plot of the velocity magnitude in a magnified longitudinal section of the cone mill with oil concentration equal to 0.70 kg/kg (70 wt%) and at operating conditions corresponding to experiment no. 1 (see Table 1).

**Table 5**

Final comparison between the mean Sauter diameter predicted by the PBM and measured experimentally for experiments no. 1, 2 and 3 and for the three disperse phase concentrations investigated in this work.

Exp.	Mayonnaise 1 (0.65 kg/kg)		Mayonnaise 2 (0,70 kg/kg)		Mayonnaise 3 (0,75 kg7kg)	
	exp. data	model pred.	exp. data	model pred.	exp. data	model pred.
1	7.206	9.530	6.587	5.180	4.647	3.180
2	8.787	9.250	5.844	4.780	4.815	2.950
3	12.364	11.99	7.713	6.130	6.063	3.830

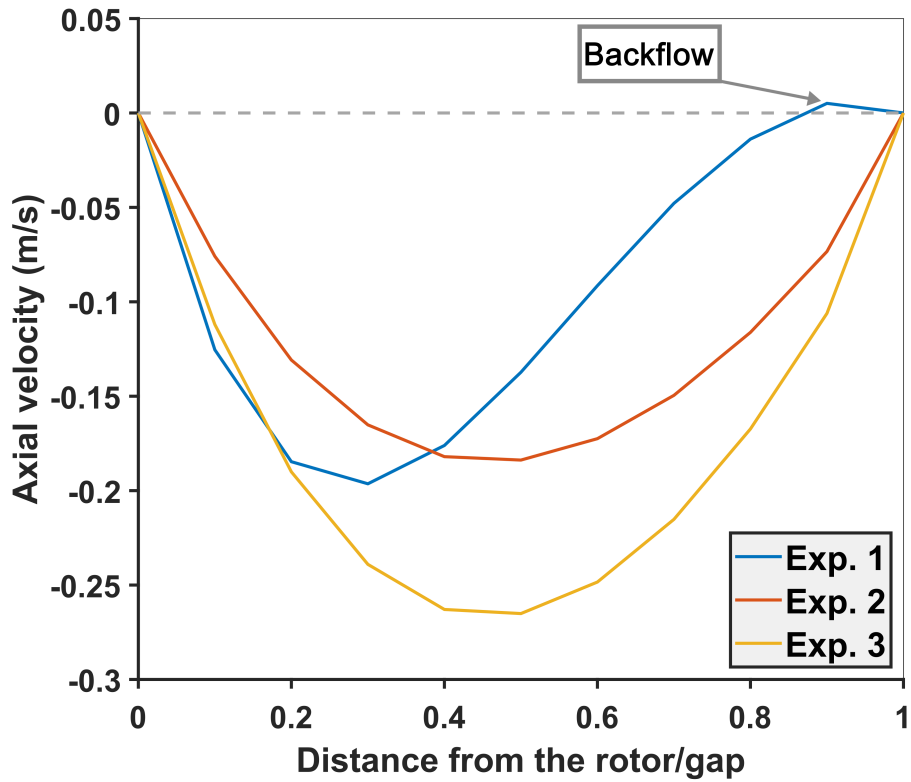


**Figure 7:** Axial velocity profiles versus the normalized distance from the rotor wall at half height of the cone mill with oil concentration equal to 0.70 kg/kg (70 wt%) and for different operating conditions (see Table 1).

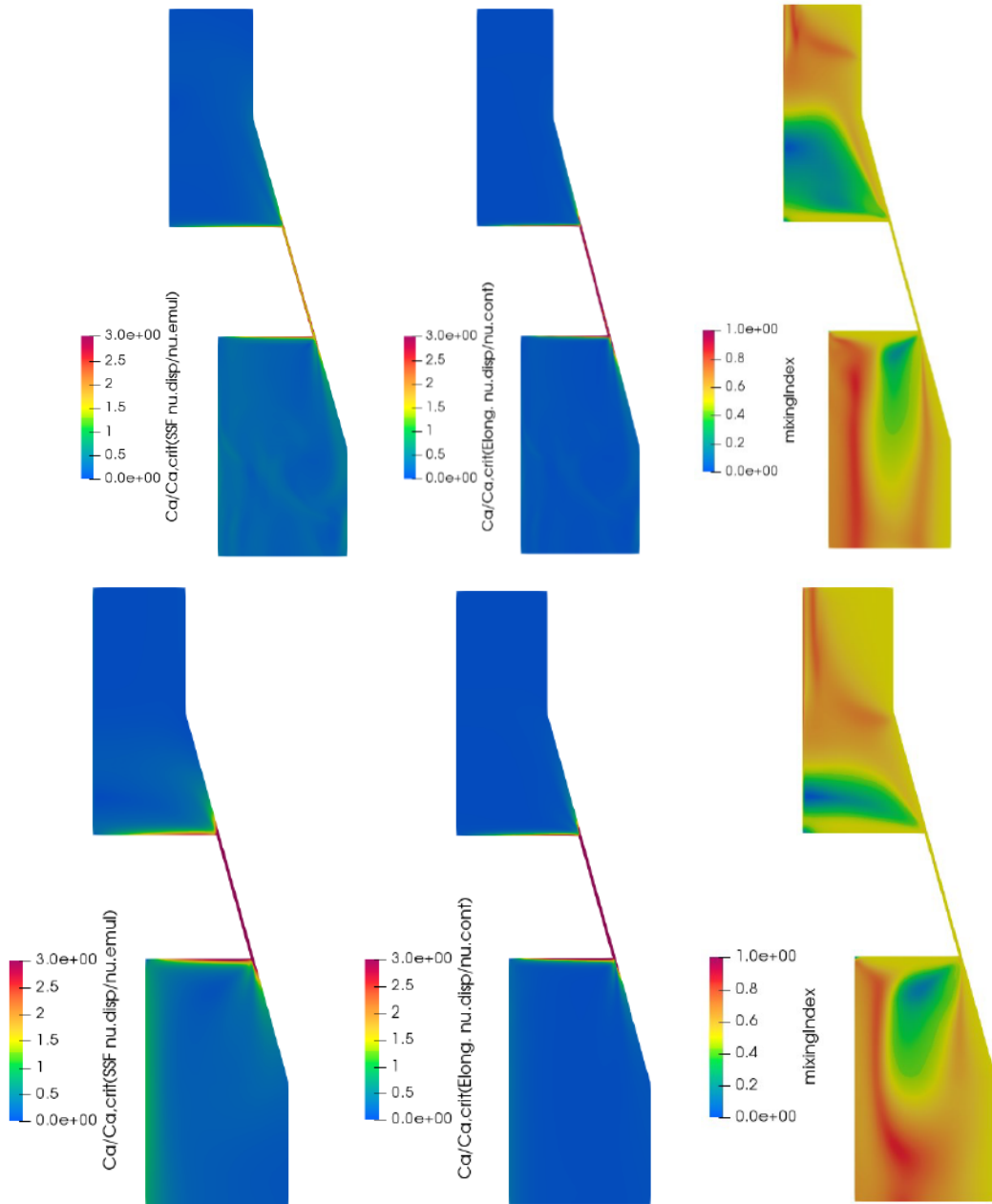


**Figure 8:** Contour plots for the ratio between the Capillary number and the critical Capillary number calculated by using the emulsion viscosity (left) and the continuous phase viscosity (center) and the mixing index,  $\alpha$  (right) for experiment no. 1 (top) and no. 3 (bottom).



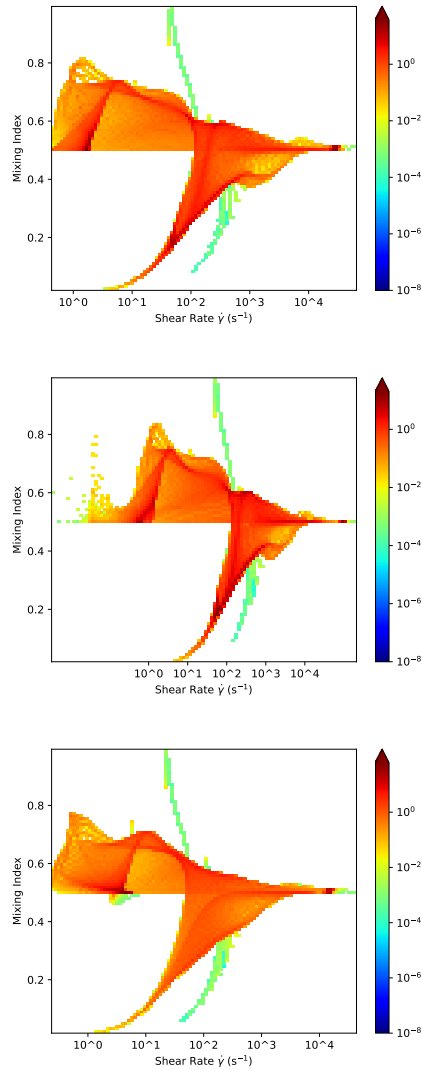


**Figure 9:** Volume distribution of mixing index (-) and shear rate (1/s) for operating conditions corresponding to experiment no. 1 (top), no. 2 (middle) and no. 3 (bottom).

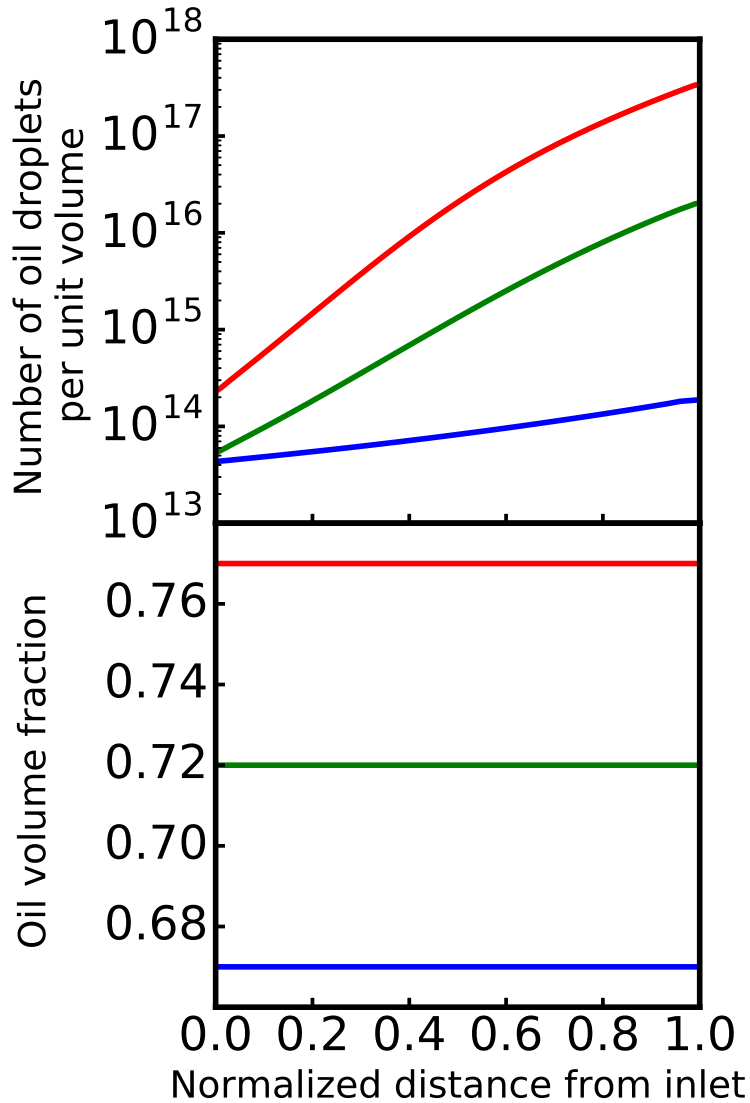


**Figure 10:** Trend of the number of oil droplets per unit volume ( $M_0$ , top) and oil volume fraction ( $\pi/6M_3$ , bottom) along the normalized distance from the middle point of inlet to the middle point of outlet of the cone mill mixer, for oil concentrations equal to 0.65 kg/kg (blue line), 0.70 kg/kg (green line), and 0.75 kg/kg (red line) in the experiment n.3 (see Table 1).

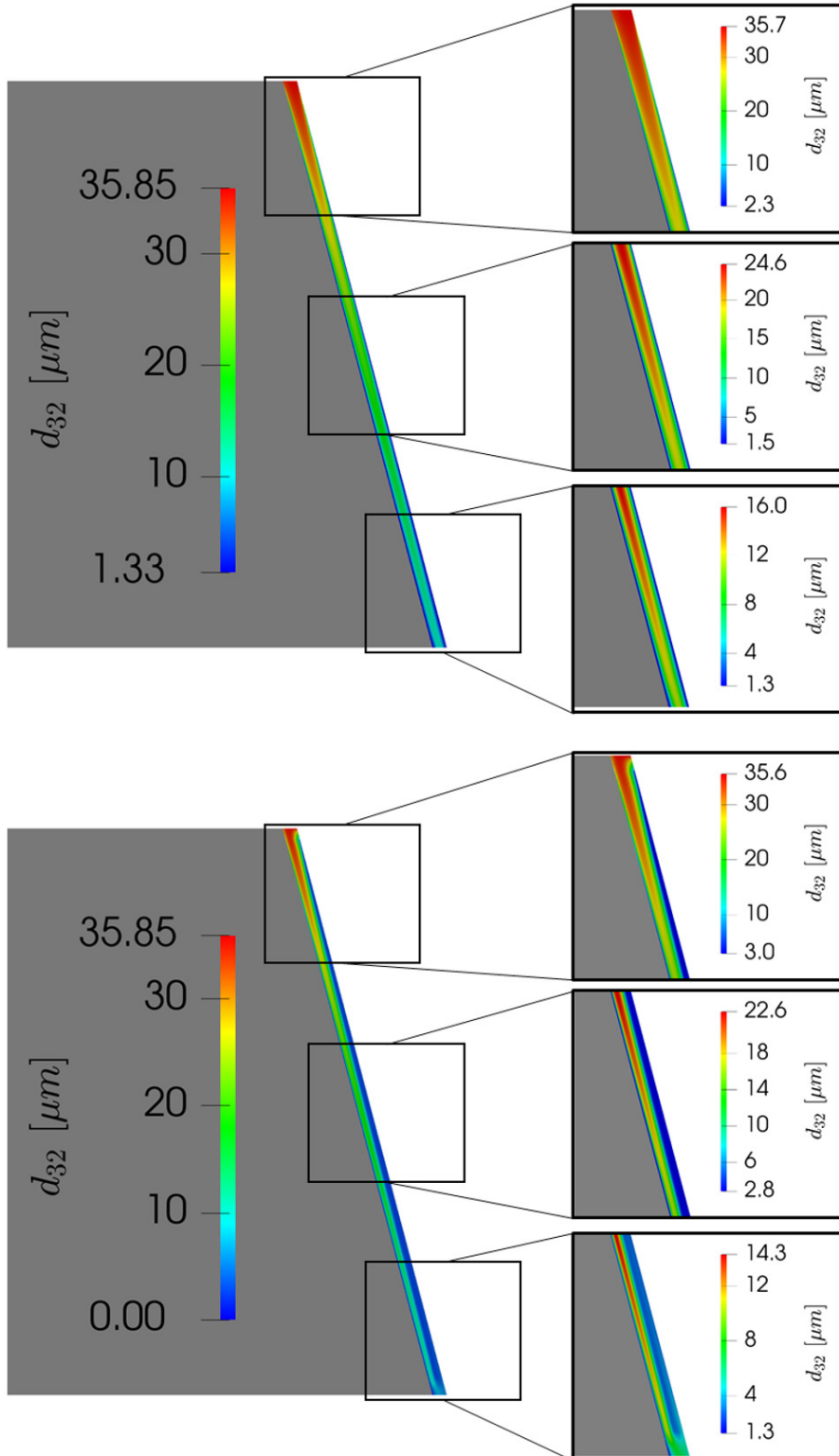


**Figure 11:** Contour plots of the mean Sauter diameter  $d_{32}$  of oil droplets along a longitudinal section of the cone mill with oil concentration equal to 0.70 kg/kg (70 wt%) for the experiments n. 3 (top) and n. 1 (bottom) (see Table 1). Insets are magnified gap sections.